Towards atom-scale spin-selective electron emitters based on strong-field Freeman resonant ionization

Shengliang Xu,[1] Qingbin Zhang,[1,*] Xianglong Fu,[1] Xiang Huang,[1] Xu Han,[1] Min Li,[1] Wei Cao,[1] and Peixiang Lu[1,2,†]

[1]*School of Physics, Huazhong University of Science and Technology, Wuhan 430074, China*

[2]*Laboratory of Optical Information Technology, Wuhan Institute of Technology, Wuhan 430205, China*

To produce electrons with well-defined spin via photoionization, realizing orbital-resolved ionization is the prerequisite due to spin-orbital coupling. In this paper, we numerically and experimentally demonstrate that the electrons emitted from two original energy degenerated orbitals ($j = 3/2$, $m = 1$ and $j = 3/2$, $m = -1$) of Xe atoms can be well separated in the energy domain through selectively achieving Freeman resonance during strong-field ionization using a circularly polarized laser field. This orbital resolved Freeman resonant ionization leads to strong spin sensitivity without the need of fine laser frequency and intensity tuning. This result enables the production of high-degree spin-polarized electrons by energy gating, which provides a unique degree of freedom for advancing many promising applications.

I. INTRODUCTION

Spin angular momentum is an intrinsic property of the electron. The ability to manipulate the spin of the electron offers a unique additional degree of freedom as well as information, simulating promising applications ranging from probing the magnetic properties of matter [1] to detecting the chiral molecular systems at ultrafast timescales [2,3]. To produce spin-polarized electrons via photoionization of a gaseous or solid target, the circularly polarized laser (CPL) field can be typically employed. The well-defined angular momentum of the photon on the direction of propagation of the CPL field is transferred to the electrons, as dictated by the dipole selection rules, leading to a spin sensitivity due to the spin-orbital coupling.

It has been demonstrated in the early studies that spin polarization (SP) can be achieved via one-photon ionization from a particular fine-structure level of an atom or a molecule driving by CPL field [4]. The extension to weak-field two-photon or three-photon ionization was also proposed shortly thereafter by Dixit *et al.* [5], Nakajima and Lambropoulos [6], and Matsuo *et al.* [7]. The basic drawback of these mechanisms is that they rely on fine tuning the frequency of a narrow bandwidth laser and simultaneously require high laser intensity for launching multiphoton processes. Actually, in the early stage, lasers were not sufficiently developed to provide the necessary tunability and monochromaticity, not to mention intensity, to make these schemes attractive.

However, things have changed since then. Laser sources of sufficient intensity and broad bandwidth (short pulse duration) have evolved dramatically and continue doing so. It is thus realistic to use a strong CPL field to directly release the spin-orbital coupled bound electrons into the continuum [8]. Since no specific intermediate state is involved, this scheme can operate for a broad range of laser frequencies and intensities. To decouple the entanglement of spin and orbital momentum for spin-polarized electrons, it was predicted in theory to utilize the sensitivity of ionization in CPL fields to the initial electron rotation in current-carrying valence orbitals [9]. For example, the fourfold degeneracy of the $P_{3/2}$ state of Xe is reduced to twofold in the CPL field, leading to a spin polarization up to 50% in theory [10] and 30% in experiment [11]. To further improve the spin polarization, efforts have been devoted to the $P_{1/2}$ state of noble Xe [12,13] and other open-shell molecules [14,15], which are only twofold degenerate. Again, due to different ionization rates for corotating and counter-rotating in CPL fields [16], the twofold degeneracy is degraded, and a higher spin polarization is reached. One may already notice that the sensitivity of ionization in the CPL field to the electron rotation in the initial orbital is pivotal to reduce the degeneracy and even obtain a high degree of spin polarization [10]. However, this is related to an intriguing question of how ionization probability depends on the rotated laser electric vectors having the same or opposite helicities to the atomic orbital. The answer is less obvious. For the weak-field one-photon direct ionization, the corotating case dominates [17,18]. For the nonadiabatic strong-field tunneling ionization, it was predicted and later confirmed both experimentally and numerically that the counter-rotating case is favored [19,20]. For multiphoton ionization (MPI), it has been demonstrated that the corotating case is dominant at low laser intensity, but at higher intensities the counter-rotating case starts to be increasingly favored [21,22].

In the present paper, we report the observation of energy splitting in photoelectron energy distribution (PEED) for two energy degenerated atomic orbitals ($j = 3/2$, $m = 1$ and $j = 3/2$, $m = -1$) in a strong CPL field. The energy splitting in PEED is demonstrated to originate from the threshold
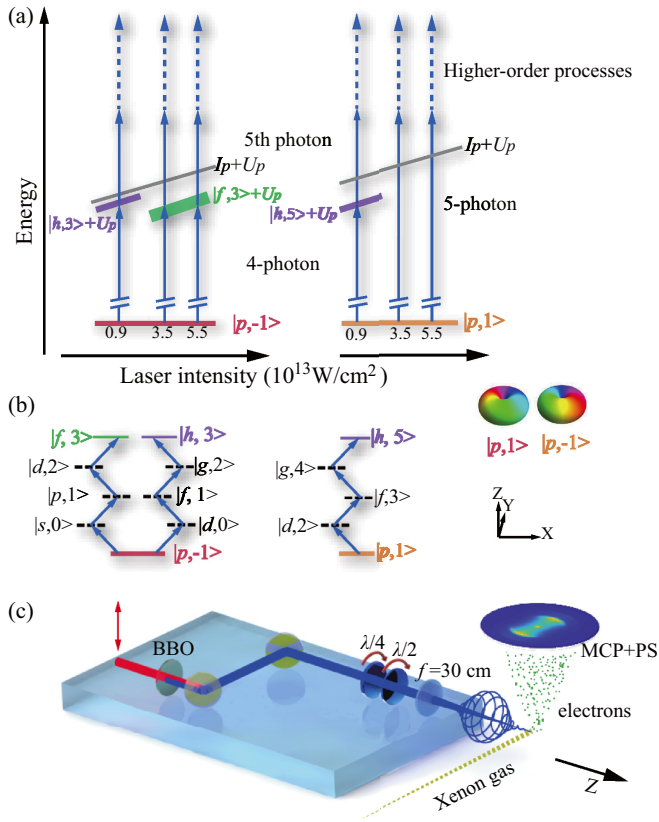
FIG. 1. (a) The schematic diagram of the ionization process for the electrons ejected from the quantum states with opposite sign of magnetic quantum number. The higher-order processes refer to absorbing more than the minimum number of photons required for ionization and are labeled by dashed arrows. (b) The resonance processes are given for electrons from the two energy-degenerated atomic orbitals ($j = 3/2$, $m = 1$ and $j = 3/2$, $m = -1$) (c) Schematic view of experimental setup. The laser pulse of 800 nm is linearly polarized. The thickness of β-barium-borate (BBO) crystal is 300 μm. The laser is focused onto the supersonic Xe gas beam by a plano-convex lens ($f = 30$ cm). The ionized electrons are subsequently focused by the electric field onto a dual multichannel plate (MCP), followed by a phosphor screen (PS) and CMOS camera.

intensities for Freeman resonance ionization and is lower for the $m = 1$ state and higher for the $m = -1$ state, which enables a considerable difference of kinetic energy of released electrons between the two ionization paths. From the observed energy splitting in PEED the quantum states of which the electrons are ionized can be identified unambiguously, which is beneficial to produce a high degree of spin-polarized electrons.

Our scheme is shown in the energy diagram as illustrated in Fig. 1(a). A right circularly polarized pulse (helicity $+1$) is used for removing the valance electron of Xe from its ground states (ionization potential $I_p = 12.13$ eV) with opposite helicities. Choosing the z axis along the incident pulse, the absorption of a photon will change the magnetic quantum number (MQN) by $+1$ monotonically. At 410 nm (photon energy $\hbar\omega = 3.03$ eV), at least five photons are required to reach the continuum. The higher-order processes refer to absorbing more than the minimum number of photons required

for ionization as shown in Fig. 1(a). The three possible pathways of four-photon resonance are (i) $|p, -1\rangle \rightarrow |s, 0\rangle \rightarrow |p, +1\rangle \rightarrow |d, +2\rangle \rightarrow |f, +3\rangle$; (ii) $|p, -1\rangle \rightarrow |d, 0\rangle \rightarrow |f, +1\rangle \rightarrow |g, +2\rangle \rightarrow |h, +3\rangle$; and (iii) $|p, +1\rangle \rightarrow |d, +2\rangle \rightarrow |f, +3\rangle \rightarrow |g, +4\rangle \rightarrow |h, +5\rangle$ as shown in Fig. 1(b), where $|l, m\rangle$ characterizes the angular part of the wave function. Following these pathways, generally, the kinetic energy of the ejected electron for MPI satisfies

$$E_k = n\hbar\omega - [I_p + U_p(I)], \qquad (1)$$

where n is the total number of photons absorbed, and $U_p = e^2 I/(2cm\epsilon_0\omega^2)$ represents the shift of ionization potential via dynamic Stark shift. According to Eq. (1), when the electrons are ionized by absorbing a certain number of photons, their kinetic energies decrease with the increase of laser intensity for the three pathways. Besides the continuum level, the Rydberg states of Xe also shift upward along with the ionization potential by approximately U_p [23]. In the nonresonant case, the accurate value of U_p can be obtained from the shift of the above-threshold ionization (ATI) peaks. The estimated error of the laser intensity calibration is 3.6%. With this method, the intensities of the 410-nm field are calibrated. Since the energies of $|h, +3\rangle$ and $|h, +5\rangle$ states are higher than that of the $|f, +3\rangle$ state, with the increase of laser intensity, the $|h, +3\rangle$ and $|h, +5\rangle$ states turn into four-photon resonance first, and the $|f, +3\rangle$ state goes into resonance later. The laser intensities required for the Stark effect to upshift the $|h, +5\rangle$ and $|h, +3\rangle$ intermediate states into four-photon resonance via pathway (iii) and (ii) are around 9×10^{12} W/cm^2 [24]. At this low intensity, ionization is still highly improbable. Instead, the $|f, +3\rangle$ states require greater intensities to be shifted into the four-photon resonance via pathway (i) according to Eq. (1), and thus have a much larger ionization rate at resonance due to the highly nonlinear ionization rate as a function of intensity [25]. As long as the laser intensity does not significantly exceed the laser intensity required for resonant ionization, the ATI process produces a photoelectron with laser intensity independent energy:

$$E_k = n\hbar\omega - (I_p - E_r), \qquad (2)$$

where E_r is the field-free energy of the resonant intermediate state. The scenario resulting in the intensity-independent ATI peak positions was suggested by the early work showing that the excited state survives longer in the laser pulse and is ionized later by multiphoton absorption [26,27]. This scenario is also confirmed by a recent experiment in which significant time delays have been observed when an intermediate resonant state is involved [28]. If the peak intensity is higher than the resonant value, the resonance condition can be fulfilled somewhere in the laser field and the electron will then remain in the resonant intermediate state for some time before the laser peak arrives. Because the high-lying Rydberg state is shifted upwards almost as much as the continuum level, it gives rise to intensity-independent peak positions. The above discussions indicate that, by using a circularly polarized laser field with suitable intensity, the pathways of ionization are sensitive to the orbital helicity of the ground electron and we can select the $|f, +3\rangle$ states through which the (4+1) resonantly enhanced multiphoton ionization occurs. In this situation, the kinetic energy of ionized electrons in pathway

(ii) will be derived from Eq. (1), while the kinetic energy of the ejected electrons in path (i) will be derived from Eq. (2). The difference in the resonant and nonresonant ionization initialized from $|p, -1\rangle$ and $|p, +1\rangle$ states will lead to the separation of the corresponding electrons in the energy domain.

II. EXPERIMENTAL METHODS

Experimentally, we have obtained full three-dimensional photoelectron momentum distribution (PMD) by applying the tomographic reconstruction to the projected PMD measured with velocity map imaging [29–31], as shown in Fig. 1(b). The laser pulses are generated from a Ti:sapphire laser system, and then they are frequency doubled to 410 nm with a 300-μm-thick β-barium-borate crystal. Recently, it was theoretically demonstrated that the fast changing pulse envelopes (with laser pulse duration <10 fs) can generate a pattern that modulates the ATI peaks [32]. We therefore carefully diagnose our lasers, ruling out the photoelectron energy distribution splits we observed in our experiment as being caused by the splitting of the laser spectrum and pulse duration. The laser pulse used in our experiment is characterized by the home-made cross-correlation frequency resolved optical gating technique. Since the measured pulse duration (full width at half maximum) is 115 fs, its envelope should not affect the structure of the ATI peak. The linearly polarized laser pulse is converted into a right circularly polarized laser pulse by passing through a $\lambda/4$ wave plate. The rotatable linearly polarized plate is used to take measurement of the laser power in different directions on the polarization plane to confirm the laser pulse is a circular polarized laser pulse.

III. RESULTS AND DISCUSSIONS

The measured PMD and PEED for Xe are shown in Fig. 2. The real situation for Xe is more complicated than what has been discussed so far: two ionic ground states $^2P_{3/2}$ (ionization potential $I_p = 12.13$ eV) and $^2P_{1/2}$ ($I_p = 13.44$ eV) could be populated when removing a valence electron from xenon [33]. At a laser intensity of $\approx 7.2 \times 10^{13}$ W/cm^2, as shown in Fig. 2(b), each ATI order contains a pair of rings spaced by 1.31 eV. Here, the laser intensity is calibrated by the shift of the ATI peaks in the nonresonant case. The inner ring is related to the more strong bounded $^2P_{1/2}$ state (by 1.31 eV), and the outer one is related to the $^2P_{3/2}$ state. A closer inspection of the white rectangle part of Fig. 2(b) reveals, very interestingly, that the first-order ATI ring associated with the $^2P_{3/2}$ ionic state exhibits a pronounced double-ring structure as shown in Fig. 2(a). In Fig. 2(c), we show the ATI energy spectrum from 0 to 6 eV. We find that the energy separation of the double-ring structure is 0.32 eV, which is much less than 1.31 eV. We therefore only concentrate on the PMD belonging to the $^2P_{3/2}$ ionic state. To understand the origin of the double-ring structure appearing in the first-order ATI, we show the PEED obtained with laser intensities spanning from 6.2×10^{13} to 7.2×10^{13} W/cm^2. For the first-order ATI displayed in Fig. 2(d), the two very prominent peaks are fixed at 2.04 and 2.36 eV in spite of the variation of the laser intensity. The measured energy separation (0.32 eV) matches very well with the energy difference between $4f$ and $5f$ states which are
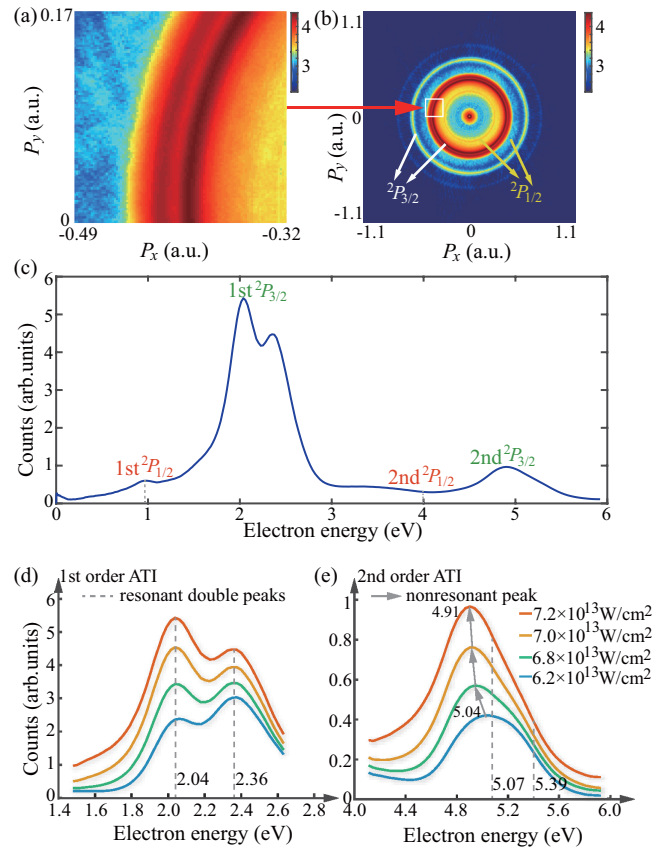

FIG. 2. (a) The enlarged view of the double-ring structure in (b). (b) The 2D photoelectron momentum distribution in the polarization plane (x-y plane) with $|P_z| < 0.92$ a.u. in logarithmic scale, generated by tomographic reconstruction. The rings belonging to two different atomic states ($j = 1/2$ and $3/2$) are labeled by the yellow and white arrows, respectively. (c) The ATI energy spectrum from 0 to 6 eV. The laser intensity is 7.2×10^{13} W/cm^2 for (a), (b), and (c). (d), (e) The measured PEED of the first-order and second-order ATI with laser intensity from 6.2×10^{13} to 7.2×10^{13} W/cm^2. The gray dashed lines are corresponding to the positions of resonance double peaks. The positions of nonresonant peaks are labeled by gray solid arrows.

available from National Institute of Standards and Technology (NIST) [34], proving the double-peak structure is contributed by the ionization from the $|p, -1\rangle$ state via resonant $|f, +3\rangle$ intermediate states. Limited by the measuring resolution of our spectrometer (0.06 eV) at 2 eV, the contributions from higher-lying f series resonance states are embedded into the high-energy tail of the main $4f$ and $5f$ resonant double-peak structure. In fact, the nonresonant ionization from the $|p, +1\rangle$ state also contributes to the first-order ATI. The peak positions estimated according to Eq. (1) are between 1.88 and 2.01 eV for the given intensities. However, we cannot recognize the nonresonant peak in the PEED, which is most likely due to the fact that the weak nonresonant peak is embedded into the strong resonant peak. The second-order ATI peaks show rather different behavior compared to the first-order ATI peaks as depicted in Fig. 2(d). In the second-order ATI, there is only one main peak and it moves continuously towards lower energy from 5.04 to 4.91 eV with the increase of laser

intensity. As is known, in principle, the second-order ATI peak should reproduce the shape of the first-order ATI peak and they should be exactly spaced by the energy of a photon.

To understand the physical mechanism behind the abnormal phenomenon, we solve the time-dependent Schrödinger equation (TDSE) for decoupling the ionization from $m = 1$ and -1 states. The time-dependent Schrödinger equation for the Xe atom is given by

$$i\partial\psi(\mathbf{r}, t)/\partial t = [-\nabla^2/2 + V_C(\mathbf{r}) + V_E(\mathbf{r}, t)]\psi(\mathbf{r}, t). \quad (3)$$

We numerically solve Eq. (3) in the length gauge with $V_E(\mathbf{r}, t) = -\mathbf{E} \cdot \mathbf{r}$. The right circularly polarized electric field $\mathbf{E}(t)$ is expressed by

$$\mathbf{E}(t) = E_0 \sin^2\left(\frac{t\pi}{\tau}\right)[\cos(\omega_0 t)\mathbf{e}_x + \sin(\omega_0 t)\mathbf{e}_y]. \quad (4)$$

Here, E_0 is the amplitude, ω_0 is the angular frequency, and τ is the total duration of the laser pulse ($\tau = 100T$; here, $T = 2\pi/\omega_0$). The effective Coulomb potential V_c of xenon is

$$V_c = -\{1 + 2\exp[-(x^2 + y^2)]\}/\sqrt{(x^2 + y^2 + 0.2)} \quad (5)$$

with the soft-core parameter 0.2, that enables us to obtain the correct energy of the valence $5p$ orbital of -0.446 a.u. (-12.13 eV). The two initial orbitals prepared for solving the TDSE are $p(m = 1) = (p_x + ip_y)/\sqrt{2}$ and $p(m = -1) = (p_x - ip_y)/\sqrt{2}$, where the basis set of p_x and p_y is obtained via the propagation of TDSE in imaginary time and additional orthogonalization procedures at each step. We utilize the split-step Fourier method to numerically solve Eq. (3) [38]. The numerical grid is integrated from $-L_0/2$ (-204.7 a.u.) to $L_0/2$ (204.7 a.u.), with a grid spacing of 0.2 a.u. for each dimension and a time step of 0.04 a.u.. The ground-state wave function is obtained via imaginary-time propagation method [39]. To avoid unphysical reflections at grid boundaries and to calculate ionization yields, the wave function in our simulation is multiplied by an absorbing function:

$$W(r) = \begin{cases} \cos\frac{(|r|-R)\pi}{2(L_0/2-R))^{1/6}}, & |r| > R \\ 1 & |r| \leqslant R. \end{cases} \quad (6)$$

Here, $R = L_0/2 - 120$. Figure 3 shows the PEED for initial $m = \pm 1$ states together with the sum of the two contributions for three different laser intensities. For each of the initial $m = 1$ and -1 states solely, the second-order ATI perfectly repeats the shape of the first-order ATI, and that is spaced exactly by one photon of energy. In Fig. 3(b), due to a ponderomotive energy shift, the ATI peak moves towards lower energy with the increase of laser intensity. However, the positions of the main two peaks are independent with laser intensity as shown in Fig. 3(a), which indicates that the resonant ionization occurs with these laser intensities. In these two-dimensional numerical calculations, we find the ATI peak splits into two subpeaks, which coincide with the resonant excitation with the two intermediate states of magnetic quantum number $m = 3$. The energies of the two intermediate states are -1.10 and -0.69 eV. The energies of the states of model Xe are obtained by diagonalizing the Hamiltonian containing model potential V_c as summarized in Table I. The positions of two resonant peaks are labeled by the gray dashed lines in Fig. 3(a). Note that the energy of the resonant double-peak structure and their
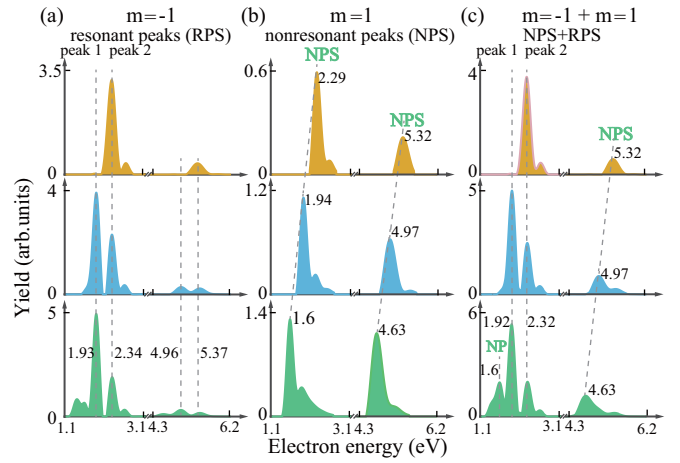

FIG. 3. (a)–(c) The simulated PEED contributed by initial $m = 1$, $m = -1$ alone, and the sum of $m = 1$ and -1 states. From the first to the third row, the laser intensities are 6×10^{13}, 8×10^{13}, and 1×10^{14} W/cm², respectively. The positions of resonant peaks and nonresonant peaks are labeled by gray dashed lines. For initial $m = 1 + m = -1$ state electrons, the nonresonant peak with the energy of 1.6 eV is labeled by gray dashed line at the laser intensity of 1×10^{14} W/cm².

energy interval differ slightly from the experimental results, because the model potential used in numerical calculation cannot perfectly reproduce all the excited-state energies compared with the NIST database. By comparing Figs. 3(a) and 3(b), it is also noticed that the first-order ATI is stronger for the resonant ionization from the $m = -1$ state, while the second-order ATI is stronger for the nonresonant ionization from the $m = 1$ state. This results in the position of the first-order ATI being fixed but the position of the second-order ATI moving with the variation of laser intensity, when the contributions from the $m = -1$ and 1 states are added, as shown in Fig. 3(c). Thus, from the different performance of the first-order and second-order ATI with the change of laser intensity we have experimentally observed in Figs. 2(c) and 2(d), it is evident that the electrons ionized from initial states with opposite helicity following different pathways have different kinetic energy. This finding provides us a unique opportunity to distinguish quantum states with opposite sign of MQN in the energy domain via Freeman resonant ionization.

We then show that the Freeman resonance ionization, which is the core for achieving orbital resolved energy splitting in PEED, is independent of the specific wavelength of

TABLE I. Energies (eV) of the first six lowest-lying eigenstates for $m = 0, \pm 1, \pm 2, \pm 3, \pm 4$.

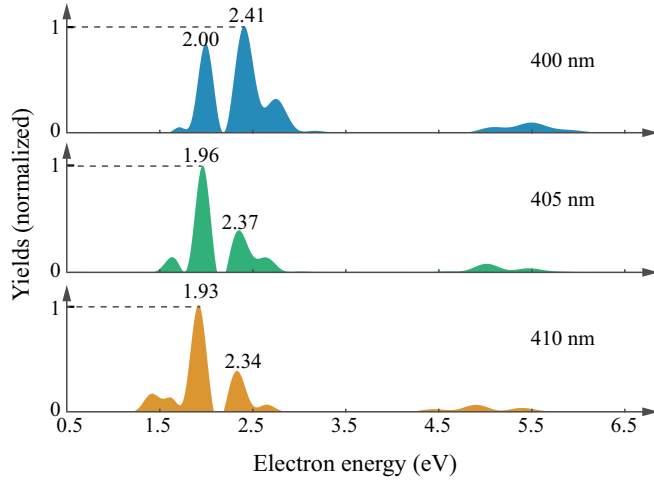| Number	$m = 0$	$m = \pm 1$	$m = \pm 2$	$m = \pm 3$	$m = \pm 4$
1	−53.90	−12.13	−2.18	−1.10	−0.67
2	−5.51	−2.94	−1.12	−0.69	−0.44
3	−2.06	−1.36	−0.67	−0.42	−0.21
4	−1.07	−0.78	−0.42	−0.16	0.11
5	−0.65	−0.49	−0.13	0.19	0.51
6	−0.38	−0.21	0.26	0.64	0.99

FIG. 4. Simulated photoelectron spectroscopy for different laser wavelengthes. The laser intensity is 8×10^{13} W/cm^2. The yield is normalized to the maximum value for every laser wavelength.
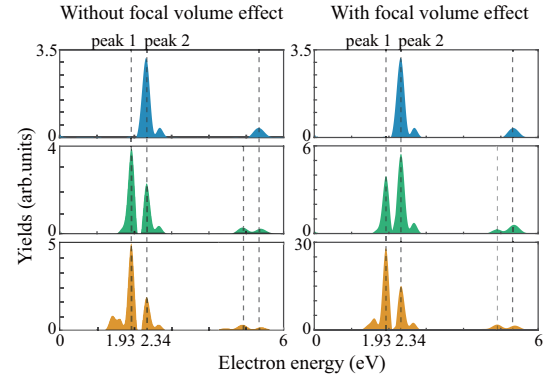

FIG. 5. The contrast of calculated photoelectron energy spectra with and without focal volume effect. The corresponding laser intensities of the blue, green, and orange photoelectron energy spectra are 6×10^{13}, 8×10^{13}, and 1×10^{14} W/cm^2, respectively.

the CPL field. The intensity of the driving CPL field is 8×10^{13} W/cm^2 and the wavelength is varied from 400 to 410 nm. For the initial $m = -1$ state, as we can see from Fig. 4, the numerically calculated energy difference (0.41 eV) of the double-peak structure for the first-order ATI remains the same with the variation of laser wavelength. This result indicates that Freeman resonant ionization occurs through the same intermediate states with different wavelengths of the driving CPL field. Therefore, the possibility of achieving Freeman ionization for selective intermediate states still holds with the variation of laser wavelength over a certain range. It is also noticed that the double-peak structure for the first-order ATI moves toward lower energy as a whole. This is because the variation of laser wavelength changes the photon energy correspondingly from 3.10 to 3.03 eV. According to Eq. (2), this changes the energy of the resonant ionization peak.

To get closer to the actual experimental laser conditions, the focal volume effect of the laser beam (the laser spot diameter before focusing is 1 cm) focused by a plano-convex lens ($f = 30$ cm) in the experiment is considered. The focused laser beam will be assumed to have the Gaussian form [35]

$$I(\rho, z) = \frac{I_0}{1 + z^2/z_r^2} \exp\left[-\frac{2\rho^2}{\omega_0^2(1 + z^2/z_r^2)} \right]. \quad (7)$$

Here, I_0 is the peak intensity, z_r is the Rayleigh range, ω_0 is the beam waist at the focus, and we define the focal point as $(\rho, z) = (0, 0)$. The beam waist at z can be expressed as

$$\omega(z) = \omega_0 \sqrt{1 + z^2/z_r^2}. \quad (8)$$

The focal volume averaged total yield of ionization at a peak intensity I_0 can be obtained by

$$Y = \int Y[I(\rho, z)]dV = \int_0^{I_0} Y(I) \frac{\partial V}{\partial I} dI, \quad (9)$$

where the volume of an isointensity shell between I and $I + dI$ is given by

$$\frac{\partial V}{\partial I} dI = \pi z_r \omega_0^2 \left\{ \frac{4(c_1 - c_2)}{3} + \frac{2(c_1^3 - c_2^3)}{9} \right.$$
$$\left. - \frac{4}{3}[\tan^{-1}(c_1) - \tan^{-1}(c_2)] \right\}. \quad (10)$$

Here, $c_1 = [\frac{I_0 - I}{I}]^{1/2}$, $c_2 = \{\frac{[I_0 - (I+dI)]}{I+dI}\}^{1/2}$, and $dI = 0.5 \times 10^{13}$ W/cm^2 in our simulation. We calculate the PEED for the initial $m = -1$ state with and without focal volume effect as shown in Fig. 5. Here, the focal volume averaged total yield of single ionization can be obtained according to Eq. (9). For the first-order ATI, the positions of peak 1 and peak 2 are labeled by gray dashed lines. It can be found that the positions of peak 1 and peak 2 for the first-order ATI remain unchanged in the cases of the laser intensities with and without focal volume effect. As the laser intensity increases, the yield of peak 1 would exceed that of peak 2 for two cases. From Fig. 5, we can find that the focal volume effect only changes the yield ratio of peak 1 and peak 2. Our result indicates that the focal volume effect does not affect the Freeman resonant ionization via the two specific intermediate states.

The ability to separate quantum states with opposite MQN in the energy domain can also be applied to generate high-degree spin-polarized electrons with high yield. Suppose we have created the Xe$^+$ in the $^2P_{3/2}$ state; the total momentum of the correlated electron of $j = 3/2$ admits both $|m_j| = 1/2$ ($m = 1$, $m_s = -1/2$ and $m = -1$, $m_s = 1/2$) and $|m_j| = 3/2$ ($m = 1$, $m_s = 1/2$ and $m = -1$, $m_s = -1/2$) of the correlated photoelectrons. Thus, the rates of spin-up ($\uparrow$, $m_s = 1/2$) and spin-down ($\downarrow$, $m_s = -1/2$) electrons are given by

$$w(\uparrow) = w(m = 1) + \frac{w(m = -1)}{3},$$

$$w(\downarrow) = \frac{w(m = 1)}{3} + w(m = -1), \quad (11)$$

where the relative weights are determined by the Clebsch-Gordan coefficients. The SP is then defined as [10,36,37]

$$\text{SP} = \frac{w(\uparrow) - w(\downarrow)}{w(\uparrow) + w(\downarrow)} = \frac{1}{2}\frac{w(m = 1) - w(m = -1)}{w(m = 1) + w(m = -1)}. \quad (12)$$
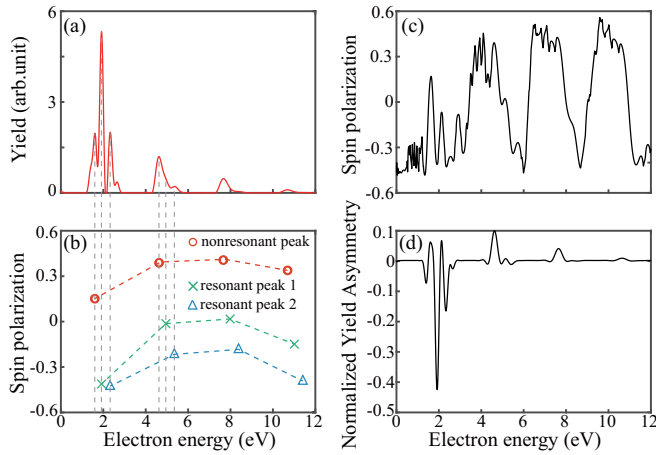
FIG. 6. (a) The photoelectron energy spectrum. (b) The spin polarization of nonresonant peaks and resonant peaks for different order ATI. The red circle, green cross, and blue triangular present nonresonant peak, resonant peak 1, and resonant peak 2. The energy difference of adjacent points on the same line is corresponding to a photon energy (3.03 eV). (c) The energy-dependent spin polarization. (d) The energy-resolved normalized yield asymmetry. The laser intensity is 1×10^{14} W/cm^2 for all results shown in this figure.

From Eq. (12) we can see that only when the electrons with specific MQN are absolutely dominant, the |SP| approaches its theoretical limit of 0.5. To see the SP of ATI peaks with high yields, we first show the photoelectron energy distributions in Fig. 6(a) at the laser intensity of 1×10^{14} W/cm^2. The SP of different order nonresonant peaks and resonant peaks is shown in Fig. 6(b). At energies of 1.93 and 2.34 eV as shown in Fig. 6(b), the SP can reach -0.412 and -0.427. This is because the electrons are contributed by the resonant ionization of the $m = -1$ state via two intermediate states at these two energies, while the nonresonantly ionized electrons are located in the lower-energy region. For the third-order ATI at an energy of 7.06 eV, however, the SP is 0.406. The reason is that the electrons at this energy are contributed mainly by the nonresonant ionization of the $m = 1$ state, and the resonant electrons are less efficient and located in the higher-energy region. When we increase the laser intensity from 1.0×10^{14} to 1.4×10^{14} W/cm^2 (not shown here), the nonresonant peak moves farther away from the resonant double peaks. Therefore, our results indicate that the absolute value of the highest spin polarization is further increased to very close to the theoretical limit of 0.5. To have a visual impression of the width of the energy window for selecting a desired degree of spin polarization with high yield, we introduce the energy-resolved SP and energy-resolved normalized yield asymmetry (NYA) in Figs. 6(c) and 6(d). Here, the NYA is defined as [40]

$$\text{NYA} = \frac{w(\uparrow) - w(\downarrow)}{\max[(w(\uparrow) + w(\downarrow)]}. \tag{13}$$

The NYA in Eq. (13) reflects the relative electron yields with different spin polarization at a specific energy. These results indicate that our method does not rely on making the ionization probabilities for initial states with opposite helicities very different to achieve a high degree of SP, since the contributions of the two states have already been separated in the energy domain. The previous experiment reported the highest SP of 0.35 for the $j = 3/2$ state, even if the ionization rate for the $m = -1$ state is already 70% higher than that of the $m = 1$ state. This is because the mixed contributions from both the $|p, -1\rangle$ and the $|p, 1\rangle$ initial states reduce the observed spin contrast [12]. In fact, the dependence of the ionization on the sign of the MQN is very sensitive to laser parameters; especially, the ionization probabilities get close at high intensity due to depletion of both of the two initial states. However, there are at least two benefits of applying relative high laser intensity in our method. First, the higher laser intensity makes the shift of the nonresonant peak in the energy domain larger; thus, it will be helpful to use a high-resolution electron monochromator (0.07 eV) [41] to gate the electrons with interested energy. Second, the higher intensity obviously results in a higher electron yield.

IV. CONCLUSION

In conclusion, we have demonstrated a scheme which reveals the initial quantum states of ionized electrons in the strong-field photoelectron energy spectrum. The separation of electrons ionized from initial states with opposite helicities is primarily attributed to counter-rotating electrons with the laser field ionized resonantly and with a fixed kinetic energy, while the corotating electron is ionized nonresonantly with a laser intensity dependent kinetic energy due to dynamic Stark shift. Our method, which mechanically does not rely on fine laser frequency and intensity tuning, is universal and can be directly applied to other atoms. Our paper will help uncover the electronic structure that determine properties of matter in the framework of the photoelectron energy spectrum. The presented method also provides an efficient way to manipulate the process of ionization and can be further applied to, for example, the detection of ring currents in single atoms [42] and the production of high-degree spin-polarized electrons [12,13].

[1] A. V. Subashiev, Yu. A. Mamaev, Yu. P. Yashin, and J. E. Clendenin, Phys. Low Dimens. Struct. **1**, 1 (1999).

[2] R. Naaman and D. H. Waldeck, Annu. Rev. Phys. Chem. **66**, 263 (2015).

[3] K. Michaeli, N. Kantor-Uriel, R. Naaman, and D. H. Waldeck, Chem. Soc. Rev. **45**, 6478 (2016).

[4] U. Fano, Phys. Rev. **178**, 131 (1969).

[5] S. N. Dixit, P. Lambropoulos, and P. Zoller, Phys. Rev. A **24**, 318 (1981).

[6] T. Nakajima and P. Lambropoulos, Europhys. Lett. **57**, 25 (2002).

[7] Y. Matsuo, N. Yonekura, T. Kobayashi, Y. Fukuyama, and T. Nakajima, Am. Meteorol. Soc. **49**, J28 (2004).

[8] H. P. Kang, C. L. Wang, Z. Y. Lin, Y. J. Chen, M. Y. Wu, W. Quan, H. P. Liu, and X. J. Liu, Chin. Phys. Lett. **28**, 832011 (2014).

[9] I. Barth and O. Smirnova, Phys. Rev. A **87**, 013433 (2013).

[10] I. Barth and O. Smirnova, Phys. Rev. A **88**, 013401 (2013).

[11] A. Hartung, F. Morales, M. Kunitski, K. Henrichs, A. Laucke, M. Richter, T. Jahnke, A. Kalinin, M. Schöffler, L. Ph. H. Schmidt, M. Ivanov, O. Smirnova, and R. Dörner, Nat. Photonics **10**, 526 (2016).

[12] D. Trabert, A. Hartung, S. Eckart, F. Trinter, A. Kalinin, M. Schöffler, L. Ph. H. Schmidt, T. Jahnke, M. Kunitski, and R. Dörner, Phys. Rev. Lett. **120**, 043202 (2018).

[13] M.-M. Liu, Y. Shao, M. Han, P. Ge, Y. Deng, C. Wu, Q. Gong, and Y. Liu, Phys. Rev. Lett. **120**, 043201 (2018).

[14] K. Liu and I. Barth, Phys. Rev. A **94**, 043402 (2016).

[15] K. Liu and I. Barth, J. Mod. Opt. **64**, 987 (2017).

[16] T. Herath, L. Yan, S. K. Lee, and W. Li, Phys. Rev. Lett. **109**, 043004 (2012).

[17] H. A. Bethe and R. Jackiw, *Intermediate Quantum Chemistry* (New York, Amsterdam, 1964).

[18] S. Askeland, S. A. Sørngård, I. Pilskog, R. Nepstad, and M. Førre, Phys. Rev. A **84**, 033423 (2011).

[19] I. Barth and O. Smirnova, Phys. Rev. A **84**, 063415 (2011).

[20] I. Barth and M. Lein, J. Phys. B **47**, 204016 (2014).

[21] J. H. Bauer, F. Mota-Furtado, P. F. O'Mahony, B. Piraux, and K. Warda, Phys. Rev. A **90**, 063402 (2014).

[22] X. Zhu, P. Lan, K. Liu, Y. Li, X. Liu, Q. Zhang, I. Barth, and P. Lu, Opt. Express **24**, 4196 (2016).

[23] R. R. Freeman, P. H. Bucksbaum, H. Milchberg, S. Darack, D. Schumacher, and M. E. Geusic, Phys. Rev. Lett. **59**, 1092 (1987).

[24] M. P. de Boer, L. D. Noordam, and H. G. Muller, Phys. Rev. A **47**, R45(R) (1993).

[25] V. Schyja, T. Lang, and H. Helm, Phys. Rev. A **57**, 3692 (1998).

[26] M. P. de Boer and H. G. Muller, Phys. Rev. Lett. **68**, 2747 (1992).

[27] A. Rudenko, K. Zrost, C. Schröter, V. L. B. de Jesus, B. Feuerstein, R. Moshammer, and J. Ullrich, J. Phys. B **37**, L407 (2004).

[28] X. Gong, C. Lin, F. He, Q. Song, K. Lin, Q. Ji, W. Zhang, J. Ma, P. Lu, Y. Liu, H. Zeng, W. Yang, and J. Wu, Phys. Rev. Lett. **118**, 143203 (2017).

[29] A. Eppink and D. H. Parker, Rev. Sci. Instrum. **68**, 3477 (1997).

[30] C. Smeenk, L. Arissian, A. Staudte, D. Villeneuve, and P. Corkum, J. Phys. B **42**, 185402 (2009).

[31] M. Wollenhaupt, M. Krug, J. Köhler, T. Bayer, C. Sarpe-Tudoran, and T. Baumert, Appl. Phys. B **95**, 647 (2009).

[32] R. Della Picca, A. A. Gramajo, C. R. Garibotti, S. D. López, and D. G. Arbó, Phys. Rev. A **93**, 023419 (2016).

[33] C. Bordas, F. Paulig, H. Helm, and D. L. Huestis, Rev. Sci. Instrum. **67**, 2257 (1996).

[34] Available at http://physics.nist.gov/cgi-bin/ASD/energy1.pl.

[35] A. M. Sayler, P. Q. Wang, K. D. Carnes, and I. Ben-Itzhak, J. Phys. B **40**, 4367 (2007).

[36] D. B. Milošević, Phys. Rev. A **93**, 051402(R) (2016).

[37] D. B. Milošević, J. Phys. B **50**, 164003 (2017).

[38] M. Feit, J. Fleck, Jr., and A. Steiger, J. Comput. Phys. **47**, 412 (1982).

[39] M. Protopapas, C. H. Keitel, and P. L. Knight, Rep. Prog. Phys. **60**, 389 (1997).

[40] K. Liu, K. Renziehausen, and I. Barth, Phys. Rev. A **95**, 063410 (2017).

[41] D. Villarejo, J. Chem. Phys. **48**, 4014 (1968).

[42] S. Eckart, M. Kunitski, M. Richter, A. Hartung, J. Rist, F. Trinter, K. Fehre, N. Schlott, K. Henrichs, L. Ph. H. Schmidt, T. Jahnke, M. Schöffler, K. Liu, I. Barth, J. Kaushal, F. Morales, M. Ivanov, O. Smirnova, and R. Dörner, Nat. Phys. **14**, 701 (2018).